

# **Estimation of the Tangential Winds and Asymmetric Structures in Typhoon Inner Core Region Using Himawari-8**

**Taiga Tsukada<sup>1</sup> and Takeshi Horinouchi<sup>1,2</sup>**

<sup>1</sup>Graduate School of Environmental Science, Hokkaido University, N10W5 Sapporo, Hokkaido, 060-0810, Japan.

<sup>2</sup>Faculty of Environmental Earth Science, Hokkaido University, N10W5 Sapporo, Hokkaido, 060-0810, Japan.

Corresponding author: Taiga Tsukada (tsukada@ees.hokudai.ac.jp)

## **Key Points:**

- The latest-generation geostationary meteorological satellites capture tropical cyclones' cloud motions that were previously unobservable
- A new method for estimating the tangential winds of tropical cyclones by using space-time Fourier analysis of satellite images is proposed
- The method was applied to Typhoon Lan (2017), and residual asymmetric motions were derived, providing a diagnosis on its intensification

## Abstract

Observations of the winds in tropical cyclones are still limited. We propose a new method for deriving the tangential winds in tropical cyclones, which employs a spectral analysis of high-frequency cloud imaging by latest-generation geostationary meteorological satellites such as Himawari-8. The method was applied to the visible images of boundary layer clouds in the eye of Typhoon Lan (2017) over an 8.5-hour period. The low-level tangential winds over the central two-thirds of the eye in radius were close to a rigid body rotation and increased with time. On its outside was a region with striating clouds rotating at much higher angular velocities, which may have been super-gradient. Asymmetric motions were visualized as the deviation from the inner rotation, and the vorticity of some mesovortices were quantified. These asymmetric motions are suggested to transport angular momentum to accelerate the inner rotation.

## Plain Language Summary

Observations of the winds in tropical cyclones (TCs) are still limited. The latest-generation geostationary meteorological satellites such as Himawari-8 capture TCs' cloud motions that were previously unobservable. We propose a method for deriving the tangential winds in tropical cyclones using a spectral analysis of high-frequency cloud imaging by these satellites. The proposed method was applied to the visible images of lower clouds in the eye of Typhoon Lan (2017) over an 8.5-hour period of daytime observations. The low-level tangential winds over the central two-thirds of the eye in radius were close to a rigid body rotation (rotational motion which has no deforming component), and its speed was increased with time. On its outside was a region with striating clouds rotating at much higher angular velocities. Asymmetric motions were visualized as the deviation from the inner rigid body rotation, and the vorticity of some mesovortices (small scale rotational features found in the TCs) were quantified. These asymmetric motions are suggested to transport angular momentum to accelerate the inner rotation. This study proves the usefulness of geostationary satellites to diagnose and study wind structures of TCs.

## 1 Introduction

Geostationary meteorological satellites seamlessly observe tropical cyclones (TCs) throughout their life cycle without interruption. Their observations are used in the Dvorak technique to estimate the intensity of TCs (Dvorak, 1975, 1984). These are also used to derive Atmospheric Motion Vectors (AMVs; see Menzel, 2001 and the references therein). AMVs are assimilated not only in global numerical weather prediction systems, but also in forecasts of TCs (Velden et al., 1998). AMVs are normally derived using the cross-correlation method (Leese et al., 1971; Schmetz et al., 1993). Even the state-of-the-art AMV products do not cover TC's inner core region (Oyama et al., 2018), presumably because the operational methods do not treat rotation.

Monitoring winds in TCs' inner core regions is important for understanding their dynamics and intensity estimation. However, conventional wind observations do not cover TCs seamlessly. Aircraft observations provide high-quality data, but their availability is limited. Ground-based Doppler radar observations are extensive (Ishihara et al., 1986; Bluestein and

Hazen., 1989; Lee et al., 1999) but limited to near their sites. Microwave scatterometers onboard low-orbit satellites and aircrafts provide sea-surface wind speeds, but saturation tends to occur under high-wind conditions (Yang et al., 2011). Surface winds estimated from satellite-borne C-band SARs may be more tolerant to saturation, but the number of the satellites suitable for this observation is limited (Mouche et al., 2017; Yu et al., 2019).

The latest-generation geostationary satellite “Himawari-8” has been operating since July 2015. Its spatio-temporal resolutions were greatly improved from its predecessor (Bessho et al., 2016). The satellite observes TCs every 2.5 minutes, which is called the target observation. The high temporal resolution is suitable to capture the rapid motions in TCs, but it has not been attempted. Since the clouds in TCs’ eyes are mostly confined in the boundary layer where the tangential winds are maximized, wind derivation from the clouds there should be useful to study and monitor TCs.

In this study, we propose a method to derive tangential winds from high-frequency imaging as done by Himawari-8. This method utilizes space-time spectral analysis to obtain tangential winds as a function of the distance from the TC center (radius) at a time resolution of  $\sim 1$  hour. It is markedly different from the conventional method using cross-correlations. Our method is especially useful to estimate winds in the lower inner core regions of TCs, as shown in section 4.

The results of the method can be used to visualize and quantify the asymmetric wind components as the deviations from the axi-symmetric components, as shown in section 5. It has been suggested numerically that the asymmetric components such as mesovortices play the important roles to intensify TCs (*e.g.*, Schubert et al., 1999; Kossin and Schubert, 2001; Hendricks et al., 2009; Naylor and Schecter, 2014). Observational studies have documented the presence of mesovortices in the TCs inner core region (*e.g.*, Fletcher et al., 1961; Muramatsu, 1986; Kossin et al., 2002; Kossin and Schubert, 2004; Shimada and Horinouchi, 2018). Some observational studies further quantified the vorticity of mesovortices in the eyewall region (Marks et al., 2008; Wingo and Knupp, 2016), but this study is the first to report a quantification of mesovortices within the eyes (section 5.1).

## 2 Data and Projection

We used visible (VIS) reflectivity at  $0.64\ \mu\text{m}$  (Band 03) from the target observations of Typhoon Lan (2017) with Himawari-8. Lan is a super typhoon that passed the Pacific Northwest region in 2017 (**Fig. 1a**). The target observation captures a TC over a  $\sim 1000\ \text{km} \times 1000\ \text{km}$  region every 2.5 minutes. Its resolution is  $0.5\ \text{km}$  at the subsatellite point. To estimate cloud-top heights, we also used the infrared (IR) brightness temperature at  $10.4\ \mu\text{m}$  (Band 13; subsatellite-point resolution:  $2\ \text{km}$ ) and the isobaric temperature and geopotential height of the Japanese 55 years Reanalysis (JRA-55) dataset (Kobayashi et al., 2015; resolution:  $1.25^\circ$ ). We defined reference vertical profiles of temperature and geopotential height at each observation time by linearly interpolating the JRA-55 data with space and time onto the TC centers. Here (only for this purpose), the TC centers were derived from the six-hourly best track data compiled by Regional Specialized Meteorological Center Tokyo (RSMC-Tokyo) by using the cubic spline interpolation with time.

100 We corrected the parallax from the entire Himawari-8 data used by equating the IR  
101 brightness temperature to the temperature in the reference profiles. The Himawari-8 data were  
102 projected onto the azimuthal equidistant projection with respect to the TC center (**Fig. 2a**). Here,  
103 since the best track is not accurate enough for this purpose, we derived the TC centers every 30  
104 minutes by subjectively examining the corrected images, and the results were interpolated with  
105 time,  $t$ , by the cubic spline interpolation (**Fig. 1c**). The projected images were sampled on the  
106 polar coordinate with the resolutions  $\Delta r = 0.5$  km along radius,  $r$ , and  $\Delta\theta = 2\pi/440$  radian  
107 along the counter-clockwise azimuth from the east,  $\theta$  (**Fig. 2b**).

108 The inner core of Typhoon Lan was observed from 21 to 22, October by GPS dropsondes  
109 during the first aircraft missions of the Tropical Cyclones-Pacific Asian Research Campaign for  
110 the Improvement of Intensity Estimations/Forecasts (T-PARCII) (Ito et al., 2018). For  
111 verification, we used a dropsonde profile obtained at  $r \sim 20$  km at around 6:50 UTC, 21.

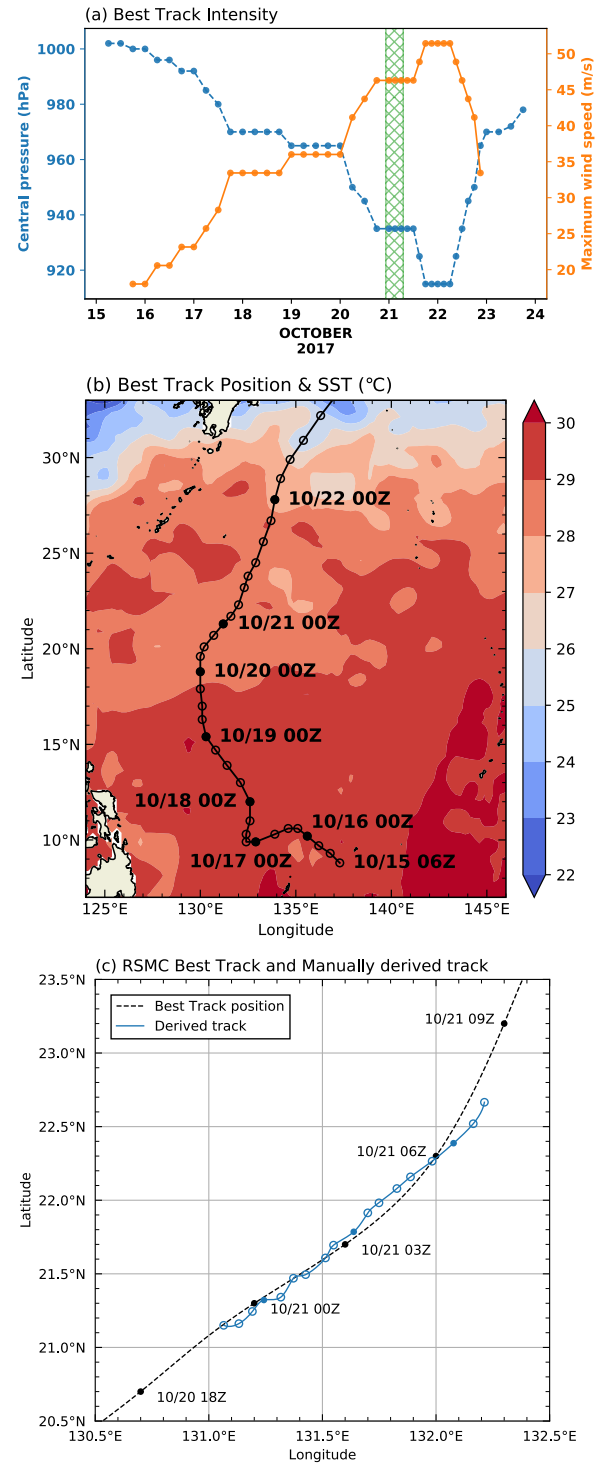
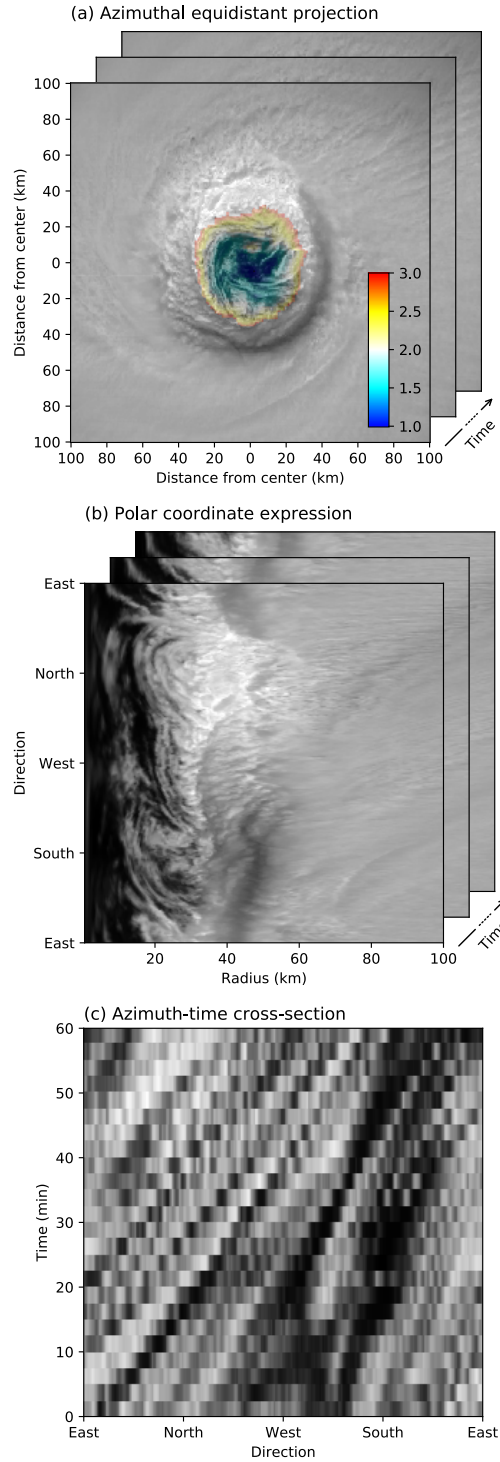


**Figure 1.** (a) Maximum 10-minute surface wind (orange circles) and central pressure (blue circles) based on the best track data by RSMC-Tokyo. The analysis period is shown by green hatches. Time is in UTC. (b) The RSMC TC center track and the mean sea surface temperature of 21, October from the daily Optimum Interpolation Sea Surface Temperature (OISST) (Banzon et al., 2016). (c) The RSMC best track (black circles) and our manually derived track (blue circles).



119

**Figure 2.** Examples of image preprocessing. **(a)** Parallax-corrected and projected VIS reflectivity (gray-scale) and estimated altitude in the eye (km; color shading). The altitudes of 0, 1, and 2 km correspond to the temperatures of 301.15, 294.15, and 290.65 K, respectively. **(b)** Brightness data on the polar coordinates. **(c)** Azimuth-time cross-section for 1 hour at a radius of 20 km.

### 3 Proposed method

The following five steps yield a tangential velocity profile  $v_E$  as a function of  $r$ . It is expected that  $v_E$  is close to the azimuthal-mean tangential wind at around the cloud top, if the TC is nearly axi-symmetric, so we shall call it the representative tangential wind. For simplicity, we assume that the rotation is counter-clockwise as in the Northern Hemisphere.

Step 1: Project image data obtained at a short time interval,  $\Delta t$ , onto the polar coordinate with respect to the TC center (e.g., **Fig. 2ab**).

Step 2: Take a time sequence over a duration of  $T$  (e.g., **Fig. 2c**), apply the standard preprocess for spectral analyses to detrend and cosine-taper with  $t$ , and conduct the Fast Fourier Transform (FFT) along  $\theta$  and  $t$  to obtain two-dimensional power spectra with angular frequency,  $\omega$ , and azimuthal wavenumber,  $k$  (e.g., **Fig. 3a**).

Step 3: Stabilize the power spectra by averaging over  $r_j - \frac{d_r}{2} \leq r \leq r_j + \frac{d_r}{2}$  at each of the radius  $r_j \equiv d_r j$ , where  $j$  is an integer, and  $d_r$  is a constant increment.

Step 4: Bin the power spectrum as a function of azimuthal phase velocity,  $c = \omega/k$ , by summing up over the area enclosed by  $c = b_i$ ,  $c = b_i + \Delta b$ ,  $k = k_{\min}$ ,  $k = k_{\max}$ , after applying the interpolation and extrapolation along  $\omega$  as described below (e.g., **Fig. 3b**). Here,  $b_i = b_{\min} + i\Delta b$  ( $i = 0, 1, \dots, n$ ) is the bin boundary,  $\omega_N \equiv \pi/\Delta t$  is the Nyquist frequency, and the other undefined symbols are constants defined in what follows. The resultant phase-velocity spectrum is normalized by the maximum value and referred to as  $f_i$ , so  $\max(f_i) = 1$  (e.g., **Fig. 3f-h**). Note that  $c$  corresponds to the angular velocity of rotation, since  $k$  is integer.

Step 5: Derive the representative tangential wind as  $v_E \equiv r_j \frac{\sum_{i=1}^n c_i w_i}{\sum_{i=1}^n w_i}$ , where  $w_i$  is the weight defined by using  $f_i$  and a threshold  $f_{\text{thresh}}$  as  $w_i = \begin{cases} f_i & (f_i \geq f_{\text{thresh}}) \\ 0 & (f_i < f_{\text{thresh}}) \end{cases}$ .

In order to accurately derive tangential winds, the TC centers used should be less than a few kilometers from the center of gravity of the lower layer in the eye. The azimuth resolution  $\Delta\theta$  must be smaller than  $\pi/k_{\max}$ . The projection described in section 2 satisfies these conditions.

The duration  $T$  should be comparable to the time scale of the variation of rotation to be quantified. However, it should also be long enough to secure a desired spectral resolution. The following guideline on parameter setting requires a first guess of the TC's angular velocity,  $c_0$ ; if it is not available, one can start with an ad hoc value to improve it iteratively. Since the frequency resolution  $\Delta\omega$  corresponds to the phase-velocity resolution  $\frac{\Delta\omega}{k} = \frac{2\pi}{Tk}, \frac{2\pi}{Tk_{\min}}$  should be smaller than  $c_0$ , which constrains the relation between  $T$  and  $k_{\min}$ . To avoid effects of vortex Rossby waves and the errors in TC-center estimation,  $k_{\min}$  should be greater than 1.

In principle,  $k_{\max}$  can be arbitrarily large, since the original image resolution provides a natural spectral cut-off. However, we found in our trial that to set

$$k_{\max} = \text{round}\left(\frac{2\pi r}{L_{\min}}\right)$$

provides better results, where  $L_{\min}$  is an empirical minimum wavelength to be treated (section 4). It makes  $k_{\max}$  as a function of  $r$ .

Now we define the interpolation and extrapolation in the step 3. To conduct the binning adequately, the phase-velocity resolution should be comparable or smaller than  $\Delta b$ . This can be achieved by subdividing the  $\omega$  grid points by  $J$  times as many and interpolating the spectra linearly with  $\omega$ , where  $J$  satisfies  $\frac{\Delta\omega}{Jk_{\min}} < \Delta b$ , so it can be set by

$$J = \text{ceil}\left(\frac{\Delta\omega}{k_{\min}\Delta b}\right).$$

The extrapolation along  $\omega$  is introduced to compensate the aliasing arising from insufficient  $\Delta t$ ; the clockwise spectral peak at  $k \sim -20$  and  $\omega \lesssim \omega_N$  in **Fig. 3a** is actually due to counter-clockwise signals at  $k \sim 20$  and  $\omega \gtrsim \omega_N$ . When cloud motions are dominated by a single angular velocity, the spectrum at  $\omega > \omega_N$  can be reproduced to some extent by repeating the spectra as in **Fig. 3b**. Here we introduce an integer parameter  $A$ , which sets the maximum  $\omega$  as  $A\omega_N$ . Because of the dominance of counter-clockwise motions in the eye, it is safe to set  $A = 2$ . Even a number greater than 2 can be used, if it is validated from the actual spectra.

The bin boundaries  $b_i = b_{\min} + i(b_{\max} - b_{\min})/n$  ( $i = 0, 1, \dots, n$ ) and the bin velocities  $c_i = b_{\min} + (2i - 1)(b_{\max} - b_{\min})/2n$  ( $i = 1, \dots, n$ ) are determined by setting the range  $(b_{\min}, b_{\max})$ , and the number of bins  $n$ . It is convenient to set  $n$  as

$$n = \text{ceil}\left(\frac{b_{\max} - b_{\min}}{\Delta b}\right) = \text{ceil}\left(\frac{b_{\max} - b_{\min}}{a_0 c_0}\right),$$

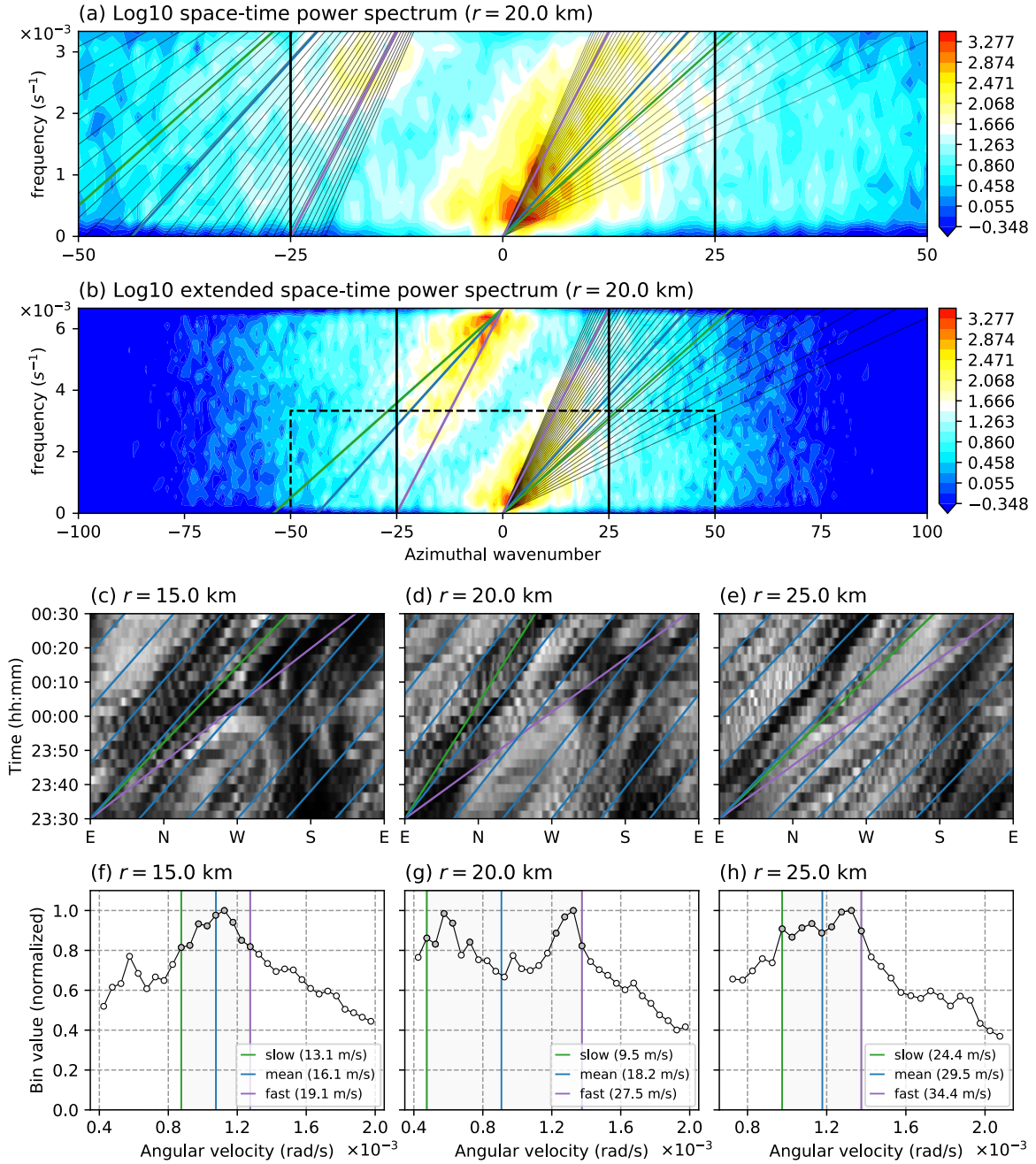
where  $a_0 \equiv \Delta b/c_0$  is the fractional increment at  $c_0$ ;  $a_0$  can be set to 0.05-0.1.

If  $A > 2$ , double counting occurs in the binning when  $k_c < k_{\max}$  and  $\omega_c < A\omega_N$ , where  $(k_c, \omega_c)$  is the intersection of  $\omega = b_{\min}k + 2\omega_N$  and  $\omega = b_{\max}k$ . This should be avoided by ensuring  $k_c \geq k_{\max}$  or  $\omega_c \geq A\omega_N$ , namely,

$$b_{\max} \leq \max\left(b_{\min} + \frac{2\omega_N}{k_{\max}}, \frac{A}{A-2}b_{\min}\right).$$

We do not have a theory to constrain the threshold  $f_{\text{thresh}}$ . Therefore, several values should be tested before it is fixed.





186

187 **Figure 3.** Examples of power spectra, azimuth-time cross-sections, and velocity binning results.  
 188 **(a)** log10 of the power spectrum at  $r = 20$  km. Black lines are drawn at  $|k| = k_{\max}$ . Gray lines  
 189 indicate bin boundaries. **(b)** Extended spectrum up to  $\omega = 2\omega_N$ . The black dashed rectangle  
 190 demarks the area shown in (a). **(c-e)** Azimuth-time cross-sections at  $r = 15, 20, 25$  km for 1  
 191 hour from 23:30 on October 20. The blue lines indicate motions at  $v_E$ , while green and purple  
 192 lines indicate those at the slowest and the fastest velocities of the top 80% bins used to derive  $v_E$ ,  
 193 respectively. **(f-h)** Binning results corresponding to (c-e). The top 80% bins are indicated by  
 194 filled gray circles.

## 4 Application to Typhoon Lan (2017)

### 4.1 Parameter setting

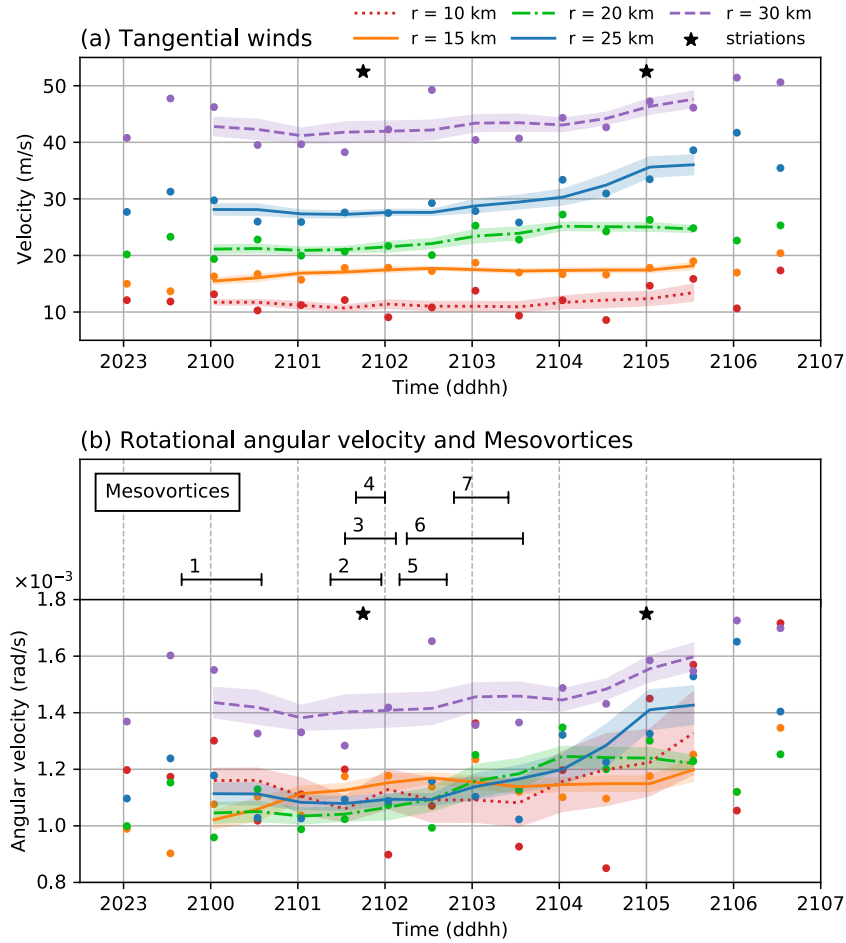
We applied the proposed method to Typhoon Lan using the VIS data over 8.5 hours since 22:30 UTC, 20, October. By the time, Lan has developed a clear eye with a radius of 35 km. We set  $T = 1$  hour, so 24 images were used for each estimation. From visual inspection,  $c_0$  was set to  $1.0 \times 10^{-3}$  rad/s. The other parameter values used are as follows:  $d_r = 5$  km;  $k_{\min} = 2$ ;  $L_{\min} = 5$  km;  $a_0 = 0.05$ ;  $J = 18$ . For  $r = 10, 15, 20$  km, we used  $A = 2$ ,  $b_{\min} = 0.4 \times 10^{-3}$  rad/s, and  $b_{\max} = 2.0 \times 10^{-3}$  rad/s (which provides  $n = 32$ ). For  $r = 25, 30$  km, we used  $A = 3$ ,  $b_{\min} = 0.7 \times 10^{-3}$  rad/s,  $b_{\max} = 2.1 \times 10^{-3}$  rad/s (which provides  $n = 28$ ). These values meet the requirements presented in section 3. We tested several values of  $f_{\text{thresh}}$  and fixed it to 0.8. **Figures 2 and 3** shown in section 3 are based on this setting.

### 4.2 Tangential wind of Typhoon Lan (2017)

**Figure 4** shows the time series of the tangential winds  $v_E$  and the rotational angular velocities  $v_E/r$  derived every 30 minutes for  $r = 10$  to 30 km (dots). The angular velocities fluctuate relatively greatly at  $r = 10$  km, which is presumably due to the frequent presence of clear air regions (e.g., **Fig. 1a**) and asymmetric velocity components as explored in section 5.2. The five-point temporal running-mean angular velocities (lines) at  $r \leq 25$  km are nearly uniform (except at  $r = 25$  km at 5–6 UTC), suggesting a high degree of horizontal mixing. The angular velocities are increased gradually through the 8.5 hours from  $\sim 1.1 \times 10^{-3}$  to  $\sim 1.2 \times 10^{-3}$  rad/s, suggesting an intensification. The rotation at  $r = 30$  km is faster throughout the analysis period. This region with  $r \sim 30$  km is characterized by striating clouds rotating at much higher angular velocities, which is investigated in sections 5.2 and 6.

To verify the results, we compared them extensively with cloud motions in the azimuth-time cross-sections like **Fig. 3c-e**. We also used movies like **Movie S1**, in which the VIS images are rotated clockwise to compensate the five-point temporal running-mean rotation at  $r = 15$  km. All these comparisons indicated the validity of our results.

Our results for  $r \leq 25$  km are consistent with the T-PARCI dropsonde data (Yamada et al., 2018). For example, the dropsonde winds obtained at  $r = 20$  km around 06:50 UTC correspond to the angular velocities around  $1.2 \times 10^{-3}$  rad/s over the altitudes between  $\sim 3$  and  $\sim 1$  km, while our result at  $r = 20$  km, 06:30:00 UTC is  $1.25 \times 10^{-3}$  rad/s.



225

226 **Figure 4.** (a) Time variation of tangential winds and (b) rotational angular velocities at the radii  
 227 of 10 (red), 15 (orange), 20 (green), 25 (blue), 30 (purple) km, respectively. Dots indicate the 30-  
 228 minute raw results, while the solid curves show the running means with time over the five  
 229 samples. The shading indicates  $\pm$  the standard error derived from the variance among the five  
 230 samples. Stars indicate the manually derived (angular) velocities of the cloud striations alongside  
 231 the eyewall. The black lines at the top of (b) show the durations when the seven mesovortices are  
 232 observed.

## 5 Quantification of asymmetric structure of TC inner core region

### 5.1 Mesovortices in the eye

**Movie S1** visualizes that the eye of Lan was full of asymmetric motions. We subjectively identified seven mesovortices (MV-1, ..., 7) at the times and locations shown in **Fig. 4b** and **5a-d**. Visual cloud tracking was performed by using traceable features with horizontal scales 1-5 km, and their vorticities relative to the background rotation was estimated from three features around mesovortices; the features are shown in supplemental figures (**Figures S1-S8**). Let their positions be  $(x_i^t, y_i^t)$  at  $t$ , where  $i = 0, 1, 2$ . From temporally intermediate positions

$$(x'_i, y'_i) = \left( \frac{x_i^{t_0} + x_i^{t_0+\Delta t}}{2}, \frac{y_i^{t_0} + y_i^{t_0+\Delta t}}{2} \right)$$

and velocities

$$(u'_i, v'_i) = \left( \frac{x_i^{t_0+\Delta t} - x_i^{t_0}}{\Delta t}, \frac{y_i^{t_0+\Delta t} - y_i^{t_0}}{\Delta t} \right),$$

the mean vorticity in the triangle is approximated by

$$\zeta = \frac{\Delta u_1 \Delta x_2 - \Delta u_2 \Delta x_1 + \Delta v_1 \Delta y_2 - \Delta v_2 \Delta y_1}{\Delta x_1 \Delta y_2 - \Delta x_2 \Delta y_1},$$

where  $(\Delta x_i, \Delta y_i) = (x'_i - x'_0, y'_i - y'_0)$  and  $(\Delta u_i, \Delta v_i) = (u'_i - u'_0, v'_i - v'_0)$ . This relation, which is exact when  $\Delta t$ ,  $\Delta x_i$ , and  $\Delta y_i$  are infinitesimal, can be derived from Stokes's theorem. The mean relative vorticities of several estimates of MV-1, 4, and 6 were obtained as  $\zeta_1 = 2.0 \times 10^{-3} \text{ s}^{-1}$ ,  $\zeta_4 = 3.2 \times 10^{-3} \text{ s}^{-1}$ , and  $\zeta_6 = -2.2 \times 10^{-3} \text{ s}^{-1}$ , respectively. Their magnitude is comparable to the background vorticity of the rotation of  $2.2 \times 10^{-3}$  to  $2.4 \times 10^{-3} \text{ s}^{-1}$ . The vorticities of MV-2, 3, 5, and 7 were not estimated due to the lack of sufficient number of concurrent traceable features.

Our result is consistent with earlier studies, since the vorticity inside the eye was increased when the mesovortices were observed. The observed asymmetric motions might have transported the high angular momentum associated with the secondary circulation into the eye.

### 5.2 Striations of the inner edge of the eyewall

The striating clouds at  $r \sim 30$  km had remarkably high angular velocities (section 4.2). They existed over a half of the inner edge of the eyewall (**Fig. 5a-d**). It has a structure similar to the "striations" or "finger-like cloud features", which have been reported several times in previous aircraft observation studies (*e.g.*, Bluestein and Marks, 1987; Aberson et al., 2006; Marks et al., 2008). We derived the angular velocity of the striations by visual inspection. The result was  $\sim 1.75 \times 10^{-3} \text{ rad/s}$  throughout the analysis period (**Fig. 4, 5e**). The striations were situated over 26-33 km from the center, and their cloud-top heights increase with  $r$  from 3 to 6 km. They tend to appear with radial orientation and are gradually tilted over time (**Fig. 5e**), which is consistent with the decrease of tangential winds with altitude.

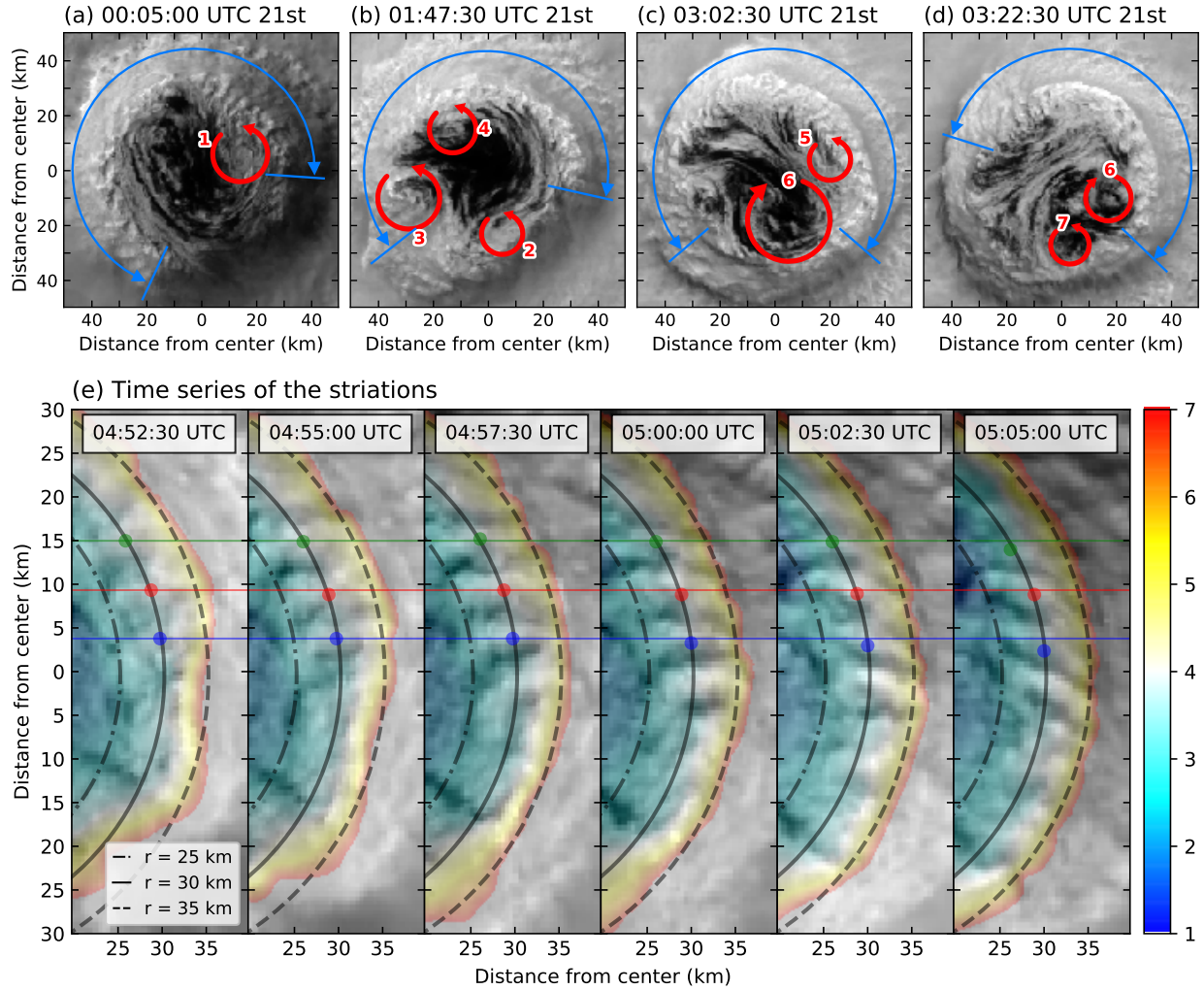


**Figure 5.** Mesovortices and striations in the eye. (a-d) VIS images at 00:05:00 UTC (a), 01:47:30 UTC (b), 03:02:30 UTC (c), 03:22:30 UTC (d), 21, October, respectively (directed north on top). Red arrows with numbers indicate the seven mesovortices, and blue arcs indicate the range of striations. (e) Time series of the striations. The VIS images were rotated clockwise at an angular velocity of  $1.75 \times 10^{-3}$  rad/s and shown every 2.5 minutes from 04:52:30 UTC, 21. Color shading indicates the estimated cloud-top heights. Black arcs show where  $r = 25, 30, 35$  km. Colored bullets show the manually identified positions of striating clouds. The colored horizontal lines are shown to indicate their positions at the same  $r$  if they are rotated at  $1.75 \times 10^{-3}$  rad/s.

## 6 Discussion

The derived rotation speed increases with  $r$  abruptly at the inner edge of the striations. This fact suggests that the striations reside in the secondary circulation that ascends in the eyewall, so the tangential winds at around the inner edge of the striations are likely super-gradient. Thus, the regularity of the striations might be due to the shear instability between the outgoing super-gradient flow and the slower flow aloft. Further studies are needed to verify it, but if this is true, it follows that the tangential winds below the striations can be even faster, since the Kelvin-Helmholtz billows move at an intermediate velocity in the shear.

The space-time spectral analysis can separate multiple velocities, so even when the upper clouds and the lower clouds overlap, the upper and lower velocities are separable, if upper clouds have gaps or are optically thin. Therefore, our method may be applicable outside the eye, after some modification. Also, it can be applied not only VIS but also to IR data.

## 7 Conclusions

We have developed a new method for estimating the tangential winds of TCs based on the space-time Fourier analysis of high-frequency geostationary satellite images. The method was applied to the 2.5-minute VIS images from Himawari-8 to quantify the rotation at the top of the atmospheric boundary layer of the eye of Typhoon Lan (2017). The rotational angular speed was nearly uniform and increased gradually with time for  $r \lesssim 25$  km. At the inner edge of the eyewall, there were striations that rotated faster than the near center rotation. It was suggested that the striations may be associated with the secondary eye-wall circulation. The flow in the eye was full of asymmetric motions, among which some mesovortices had vorticity whose magnitude is comparable to the vorticity associated with the rotation of the eye. It was suggested that the asymmetric motions transported angular momentum inward to intensify the near center rotation. Our results demonstrate the usefulness of geostationary satellite observations to diagnose and study TCs.

## Acknowledgments

The Himawari-8 data we used are downloaded from the NICT Science Cloud. The data are publicly available upon registration through the contact address shown in [https://sc-web.nict.go.jp/sc\\_staff.html](https://sc-web.nict.go.jp/sc_staff.html). The typhoon best track data by the RSMC-Tokyo is available online at <https://www.jma.go.jp/jma-eng/jma-center/rsmc-hp-pub-eg/besttrack.html>. We thank Drs. Hiroyuki Yamada and Kazuhisa Tsuboki for discussion and information on the T-PARCII dropsonde observation. Details of the T-PARCII can be found at [http://www.rain.hyarc.nagoya-u.ac.jp/~tsuboki/kibanS/index\\_kibanS\\_eng.html](http://www.rain.hyarc.nagoya-u.ac.jp/~tsuboki/kibanS/index_kibanS_eng.html). The authors declare no competing interests. This work was supported partially by the JSPS Grant-in-aid 19H00705.

## References

- Aberson, S. D., Black, M., Montgomery, M. T., and Bell, M. (2006). Hurricane Isabel (2003): New insights into the physics of intense storms. Part II—Extreme localized wind, *Bull. Am. Meteorol. Soc.*, 87(10), 1349–1354. <https://doi.org/10.1175/BAMS-87-10-1349>
- Banzon, V., Smith, T. M., Chin, T. M., Liu, C., and Hankins, W. (2016). A long-term record of blended satellite and in situ sea-surface temperature for climate monitoring, modeling and environmental studies. *Earth Syst. Sci. Data*, 8, 165–176. <https://doi.org/10.5194/essd-8-165-2016>
- Bessho, K., et al., (2016). An introduction to Himawari-8/9—Japan’s new-generation geostationary meteorological satellites. *J. Meteor. Soc. Japan*, 94, 151–183, <https://doi.org/10.2151/jmsj.2016-009>
- Bluestein, H. B., and Marks, F. D. (1987). On the structure of the eyewall of Hurricane Diana (1984): Comparison of radar and visual characteristics. *Mon. Wea. Rev.*, 115, 2542–2552. [https://doi.org/10.1175/1520-0493\(1987\)115<2542:OTSOTE>2.0.CO;2](https://doi.org/10.1175/1520-0493(1987)115<2542:OTSOTE>2.0.CO;2)
- Bluestein, H. B., and Hazen, D. S. (1989). Doppler radar analysis of a tropical cyclone over land: Hurricane Alicia (1983) in Oklahoma. *Mon. Wea. Rev.*, 117, 2594–2611. [https://doi.org/10.1175/1520-0493\(1989\)117<2594:DRAOAT>2.0.CO;2](https://doi.org/10.1175/1520-0493(1989)117<2594:DRAOAT>2.0.CO;2)
- Dvorak, V. F. (1975). Tropical cyclone intensity analysis and forecasting from satellite imagery. *Mon. Wea. Rev.*, 103, 420–430. [https://doi.org/10.1175/1520-0493\(1975\)103<0420:TCIAAF>2.0.CO;2](https://doi.org/10.1175/1520-0493(1975)103<0420:TCIAAF>2.0.CO;2)
- Dvorak, V. F. (1984). Tropical cyclone intensity analysis using satellite data. NOAA Tech. Rep. 11, 47 pp.
- Fletcher, R. D., Smith, J. R., and Bundgaard, R. C. (1961). Superior photographic reconnaissance of tropical cyclones. *Weatherwise*, 14, 102–109. <https://doi.org/10.1080/00431672.1961.9930014>
- Hendricks, E. A., Schubert, W. H., Taft, R. K., Wang, H., Kossin, J. P. (2009). Life cycles of hurricane-like vorticity rings. *J. Atmos. Sci.*, 66, 705–722. <https://doi.org/10.1175/2008JAS2820.1>
- Ishihara, M., Yanagisawa, Z., Sakakibara, H., Matsuura, K., and Aoyagi, J. (1986). Structure of a typhoon rainband observed by two Doppler radars. *J. Meteor. Soc. Japan*, 64, 923–938. [https://doi.org/10.2151/jmsj1965.64.6\\_923](https://doi.org/10.2151/jmsj1965.64.6_923)
- Ito, K., et al. (2018). Analysis and Forecast Using Dropsonde Data from the Inner-Core Region of Tropical Cyclone Lan (2017) Obtained during the First Aircraft Missions of T-PARCII. *SOLA*, 14, 105–110. <https://doi.org/10.2151/sola.2018-018>
- Kobayashi, S., et al. (2015). The JRA-55 reanalysis: General specifications and basic characteristics. *J. Met. Soc. Japan*, 92(1), 5–48. <https://doi.org/10.2151/jmsj.2015-001>
- Kossin, J. P., and Schubert, W. H. (2001). Mesovortices, polygonal flow patterns, and rapid pressure falls in hurricane-like vortices. *J. Atmos. Sci.*, 58, 2196–2209. [https://doi.org/10.1175/1520-0469\(2001\)058<2196:MPFPAR>2.0.CO;2](https://doi.org/10.1175/1520-0469(2001)058<2196:MPFPAR>2.0.CO;2)



- Kossin, J. P., McNoldy, B. D., and Schubert, W. H. (2002). Vortical swirls in hurricane eye clouds. *Mon. Wea. Rev.*, 130, 3144–3149. [https://doi.org/10.1175/1520-0493\(2002\)130<3144:VSIHEC>2.0.CO;2](https://doi.org/10.1175/1520-0493(2002)130<3144:VSIHEC>2.0.CO;2)
- Kossin, J. P., and Schubert, W. H. (2004). Mesovortices in Hurricane Isabel. *Bull. Amer. Meteor. Soc.*, 85, 151–153.
- Lee, W. -C., Jou, B. J. -D., Chang, P.-L., and Deng, S.-M. (1999). Tropical cyclone kinematic structure retrieved from single-Doppler radar observations. Part I: Interpretation of Doppler velocity patterns and the GBVTD technique. *Mon. Wea. Rev.*, 127, 2419–2439. [https://doi.org/10.1175/1520-0493\(1999\)127<2419:TCKSRF>2.0.CO;2](https://doi.org/10.1175/1520-0493(1999)127<2419:TCKSRF>2.0.CO;2)
- Leese, J. A., Novak, C. S., Clarke, and B. B. (1971). An automated technique for obtaining cloud motion from geosynchronous satellite data using cross-correlations. *J. Appl. Meteorol.* 10, 118–132. [https://doi.org/10.1175/1520-0450\(1971\)010<0118:AATFOC>2.0.CO;2](https://doi.org/10.1175/1520-0450(1971)010<0118:AATFOC>2.0.CO;2)
- Marks, F. D., Black, P. G., Montgomery, M. T., and Burpee, R. W. (2008). Structure of the eye and eyewall of Hurricane Hugo (1989). *Mon. Wea. Rev.*, 136, 1237–1259. <https://doi.org/10.1175/2007MWR2073.1>
- Menzel, W. P. (2001). Cloud tracking with satellite imagery: From the pioneering work of Ted Fujita to the present. *Bull. Amer. Meteor. Soc.*, 82, 33–48. [https://doi.org/10.1175/1520-0477\(2001\)082<0033:CTWSIF>2.3.CO;2](https://doi.org/10.1175/1520-0477(2001)082<0033:CTWSIF>2.3.CO;2)
- Mouche, A. A., Chapron, B., Zhang, B., Husson, R. (2017). Combined co- and cross-polarized SAR measurements under extreme wind conditions. *Remote Sens.*, 55, 6746–6755. <https://doi.org/10.1109/TGRS.2017.2732508>
- Muramatsu, T. (1986). The structure of polygonal eye of a typhoon. *J. Meteor. Soc. Japan*, 64, 913–921. [https://doi.org/10.2151/jmsj1965.64.6\\_913](https://doi.org/10.2151/jmsj1965.64.6_913)
- Naylor, J., and Schecter, D. A. (2014). Evaluation of the impact of moist condition on the development of asymmetric inner core instabilities in simulated tropical cyclones. *J. Adv. Model. Earth Syst.*, 6, 1027–1048. <https://doi.org/10.1002/2014MS000366>
- Oyama, R., Sawada, M., and Shimoji, K. (2018). Diagnosis of tropical cyclone intensity and structure using upper tropospheric atmosphere motion vectors. *J. Meteor. Soc. Japan*, 96B, 3–16. <https://doi.org/10.2151/jmsj.2017-024>
- Schmetz, J., Holmlund, K., Hoffman, J., Strauss, B., Mason, B., Gaertner, V., Koch, A., and Van Der Berg L. (1993). Operational cloud motion winds from Meteosat infrared images. *J. Appl. Meteor.*, 32, 1206–1255. [https://doi.org/10.1175/1520-0450\(1993\)032<1206:OCMWFM>2.0.CO;2](https://doi.org/10.1175/1520-0450(1993)032<1206:OCMWFM>2.0.CO;2)
- Schubert, W. H., Montgomery, M. T., Taft, R. K., Guinn, T. A., Fulton, S. R., Kossin, J. P., and Edwards, J. P. (1999). Polygonal eyewalls, asymmetric eye contraction, and potential vorticity mixing in hurricanes. *J. Atmos. Sci.*, 56, 1197–1223. [https://doi.org/10.1175/1520-0469\(1999\)056<1197:PEAECA>2.0.CO;2](https://doi.org/10.1175/1520-0469(1999)056<1197:PEAECA>2.0.CO;2)
- Shimada, U., and Horinouchi, T. (2018). Reintensification and Eyewall Formation in Strong Shear: A Case Study of Typhoon Noul (2015). *Mon. Wea. Rev.*, 146(9), 2799–2817. <https://doi.org/10.1175/MWR-D-18-0035.1>



- 392 Velden, C. S., Olander, T. L., and Wanzong, S. (1998). The impact of multispectral GOES-8  
393 wind information on Atlantic tropical cyclone track forecasts in 1995. Part I: Dataset  
394 methodology, description, and case analysis. *Mon. Wea. Rev.*, 126, 1202–1218.  
395 [https://doi.org/10.1175/1520-0493\(1998\)126<1202:TIOMGW>2.0.CO;2](https://doi.org/10.1175/1520-0493(1998)126<1202:TIOMGW>2.0.CO;2)
- 396 Wingo, S. M., and Knupp, K. R. (2016). Kinematic structure of mesovortices in the eyewall of  
397 Hurricane Ike (2008) derived from ground-based dual-Doppler analysis. *Mon. Wea. Rev.*,  
398 144, 4245–4263. <https://doi.org/10.1175/MWR-D-16-0085.1>
- 399 Yamada, H., Tsuboki, K., Nagahama, N., Shimizu, K., Ohigashi, T., Shinoda, T., and Nakazawa,  
400 T. (2018). Double Warm-Core Structure of Typhoon Lan (2017) as Observed through  
401 Upper-Tropospheric Aircraft Reconnaissance during T-PARCII. Preprints, 33rd  
402 Conference on Hurricanes and Tropical Meteorology, Ponte Vedra Beach, Amer. Meteor.  
403 Soc.,  
404 [https://ams.confex.com/ams/33HURRICANE/webprogram/Manuscript/Paper339931/201](https://ams.confex.com/ams/33HURRICANE/webprogram/Manuscript/Paper339931/201804_HurricaneConf_Yamada_extendAbst.pdf)  
405 [804\\_HurricaneConf\\_Yamada\\_extendAbst.pdf](https://ams.confex.com/ams/33HURRICANE/webprogram/Manuscript/Paper339931/201804_HurricaneConf_Yamada_extendAbst.pdf)
- 406 Yang, X., Li, X., Zhang, Q., Gu, X., Pichel, W. G., and Li, Z. (2011). Comparison of ocean-  
407 surface winds retrieved from QuikSCAT scatterometer and Radarsat-1 SAR in offshore  
408 waters of the U. S. west coast. *Remote Sens. Lett.*, 8, 163–167.  
409 <https://doi.org/10.1109/LGRS.2010.2053345>
- 410 Yu, P., Johannessen, J. A., Yan, X. -H., Geng, X., Zhong, X., Zhu, L. (2019). A study of the  
411 intensity of tropical cyclones Idai using dual-polarization Sentinel-1 data. *Remote Sens.*,  
412 11(23), 2837. <https://doi.org/10.3390/rs11232837>